# Structural and chemical characterization of the hardening phase in biodegradable Fe–Mn–Pd maraging steels

F. Moszner
*Laboratory of Metal Physics and Technology, Department of Materials, ETH Zurich, 8093 Zurich, Switzerland*

S.S.A. Gerstl
*Electron Microscopy ETH Zurich (EMEZ), ETH Zurich, 8093 Zurich, Switzerland*

P.J. Uggowitzer and J.F. Löffler[a)]
*Laboratory of Metal Physics and Technology, Department of Materials, ETH Zurich, 8093 Zurich, Switzerland*

(Received 28 January 2014; accepted 28 March 2014)

Fe–Mn–Pd alloys are promising candidates as biodegradable material for use in temporary implant applications. In this study, the hardening phase of Fe-rich martensitic alloys containing 1, 3, and 6 wt.% Pd and a fixed Mn content of 10 wt.% was investigated. All of these alloys show considerable age-hardening upon isothermal aging at 500 °C, exhibiting a behavior characteristic of maraging steels. Atom probe tomography (APT) and x-ray diffraction (XRD) measurements were performed to characterize the composition and crystallography of nanometer-sized precipitates forming in the overaged region of the Fe–Mn–Pd alloys. The precipitates consist mainly of Mn and Pd and the peaks of the intermetallic particles observed in the XRD spectra can be ascribed to the face-centered tetragonal $\beta_1$-MnPd phase. The precipitation sequence for Fe–Mn–Pd is revealed to be similar to that reported for Fe–Mn–Ni and Fe–Mn–Pt maraging steels.

## I. INTRODUCTION

Biodegradable metals have received significant scientific interest in recent years and Fe-based alloys are considered promising candidates.[1,2] In animal studies, the potential of pure Fe was evaluated and it was noted that the main drawback of Fe is its slow in vivo degradation rate.[3–5] According to a design strategy based on metallurgical, electrochemical, and toxicological considerations, Schinhammer et al.[2] developed novel biodegradable Fe–Mn–Pd steels. These alloys were found to exhibit increased in vitro degradation rates compared to pure Fe. Furthermore, an appropriate biocompatibility was evaluated in cytotoxic investigations of Fe–Mn,[6] Fe–Pd,[7] and Fe–Mn–C–(Pd)[8] alloys.

In addition to enhanced degradation rates, high mechanical strength would also be beneficial, so that smaller implant dimensions can be used and thus less material needs to degrade. In the case of Fe-based alloys, maraging steels reveal ultrahigh strength, which is based on the formation of intermetallic precipitates forming in the martensitic matrix during an aging treatment at temperatures between 300 and 500 °C.[9] Moszner et al.[10] observed that the martensitic alloy Fe–10Mn–1Pd (in wt.%) exhibits all features characteristic of maraging steels and that considerable age-hardening is achieved through the formation of nanometer-sized precipitates rich in Mn and Pd. For this alloy, an interesting combination of strength and ductility was observed in the overaged state (see Fig. 1). Thus, the potentially attractive electrochemical and biological characteristics, in combination with the suitable mechanical performance, make the material very interesting for biodegradable implant applications. For further alloy optimization, the structural and chemical nature of the precipitates, in particular in the overaged state, is, however, of significant interest.

It is known that the iron-rich martensite alloys of the ternary systems Fe–Mn–Ni and Fe–Mn–Pt also exhibit a maraging behavior.[10–12] Due to its technological relevance, the Fe–Mn–Ni system has been extensively studied,[11,13–22] and for this system the precipitation sequence suggested can be summarized as follows: (i) in the initial aging stage the formation of coherent NiMn body-centered-cubic (bcc) zones (A2 or B2) takes place[11,14,18]; (ii) at later stages of aging (overaged region) θ-NiMn intermetallic precipitates with a face-centered tetragonal (fct) structure form[13–15,17,18,20] (however, Kardonskii et al.[11] proposed the formation of $Ni_3Mn$ and Singh et al.[22] the formation of bcc NiMn); and (iii) on prolonged aging the precipitates redissolve and the final equilibrium microstructure only consists of austenite and ferrite (or martensite).[14] For the Fe–Mn–Pt system, Tanaka et al.[12] proposed a similar precipitation sequence, i.e., the formation of coherent bcc PtMn zones (B2) at the initial stages of aging and ordered

a)Address all correspondence to this author.
e-mail: joerg.loeffler@mat.ethz.ch
DOI: 10.1557/jmr.2014.84

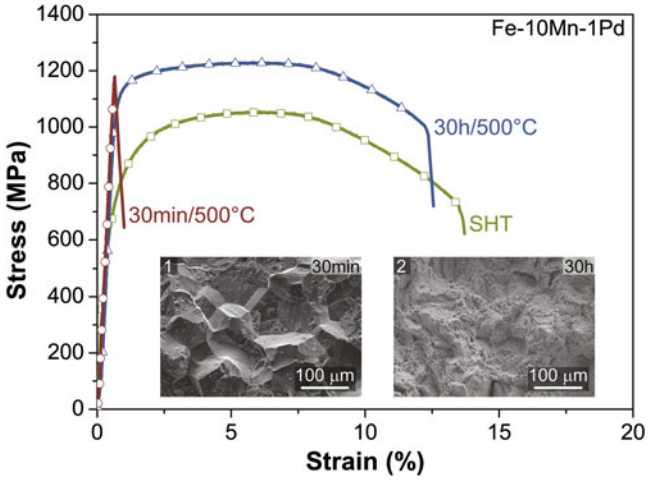


FIG. 1. Engineering stress–strain curves of Fe–10Mn–1Pd in the initial SHT state and after isothermal aging at 500 °C for 30 min (peak-aged) and 30 h (overaged).[24] A ductile behavior is seen in the SHT condition and in the overaged case. The yield strength of the alloy in the overaged state (1076 ± 6 MPa) is much larger than that of the SHT state (662 ± 13 MPa). Brittle failure results for the material in the peak-aged condition. The insert shows SEM pictures of fracture surfaces from the tensile specimens of the alloy in the peak-aged (1) and overaged (2) conditions. Intergranular fracture, which occurs along prior austenite grain boundaries, is visible in the peak-aged state, and a ductile dimple fracture is apparent in the overaged case.

fct $\beta_1$-PtMn intermetallic precipitates in the overaged regime.[12] In contrast to the Fe–Mn–Ni system, the dissolution of the particles on prolonged aging was not observed for the Fe–Mn–Pt alloys, which was ascribed to the higher bonding affinity of Mn with Pt.[12,23] In the Fe–Mn–Pd system, we suggested[10] the formation of coherent zones rich in Mn and Pd in the initial stages of aging. However, the structure of the precipitates in the overaged state has yet not been clarified, which is our aim in the present work.

For this reason, alloys with a Pd concentration of 1, 3, and 6 wt.% and a fixed Mn content of 10 wt.% were studied. The steels were isothermally aged at 500 °C and the mechanical properties as a function of aging time were investigated. The crystallography of the evolving precipitates was characterized by x-ray diffraction (XRD), and atom probe tomography (APT) was performed to analyze their chemical composition.

## II. EXPERIMENTAL

Casts of 80 g were prepared from pure elements (Fe: Armco; Mn: 99.9% pure, Alfa Aesar, Germany; Pd: 99.95% pure, UBS, Switzerland) by vacuum induction-melting under argon atmosphere (purity: 99.998%). Prior to the homogenization treatment, the ingots were encapsulated in quartz tubes also under argon atmosphere. The solution-heat-treatment (SHT) of Fe–10Mn–1Pd was performed at 1250 °C for 12 h,[10] and for Fe–10Mn–3Pd and Fe–10Mn–6Pd at 1400 °C for 1 h under argon atmosphere, followed by water quenching. The higher SHT temperature for the steels containing 3 and 6 wt.% was chosen because SEM investigations of Fe–10Mn–3Pd revealed that such a temperature is required to obtain a homogenous microstructure. Isothermal aging of the SHT specimens was conducted at 500 °C in air for various durations (up to 1200 h), followed by quenching in water. Prior to aging of the samples for 1200 h at 500 °C, they were sealed in quartz tubes under argon atmosphere to prevent oxidation. To follow the aging process of the heat-treated materials, Vickers hardness measurements were performed using a Brickers 220 hardness tester (Gnehm, Switzerland).

For the preparation of tensile test specimens of Fe–10Mn–1Pd, an ingot of 1 kg was prepared which was forged and swaged to produce rods having a diameter of 6 mm.[24] The finial SHT of this material was conducted at 1150 °C for 12 h under argon atmosphere followed by water quenching. Stress–strain curves were recorded via standard[25] tensile testing (Schenck-Trebel, Germany), using cylindrical specimens of 2 mm diameter with a gage length of 12 mm at a strain rate of $10^{-3}$ $s^{-1}$.

The microstructure of Fe–10Mn–*x*Pd ($x$ = 1, 3, 6) samples etched with 1 vol% nitric acid in water was investigated using optical microscopy (OM, Reichert-Jung Polyvar Met, Reichert Inc., Depew, NY), and scanning electron microscopy (SEM) was performed with a Hitachi SU-70 (Hitachi High-Technologies Corporation, Tokyo, Japan), equipped with an X-max energy-dispersive x-ray (EDX) detector (Oxford Instruments, Oxford Instruments plc, UK). For phase identification, XRD measurements (PANalytical X'Pert Pro, PANalytical Co., Netherlands) were conducted using Cu $K_\alpha$ ($\lambda$ = 0.15406 nm) radiation, operating at 45 kV and 40 mA with a step size of 0.03° and a time interval of 12 s, and a diffracted beam monochromator to reduce fluorescence effects. Specimens of all alloys aged for 30 h at 500 °C were analyzed via APT. For this, bars of 0.3 × 0.3 × 15 $mm^3$ were cut from the aged ingots and needle-shaped specimens were obtained by electrochemical polishing via a standard two-step process.[10,26] The APT measurements of Fe–10Mn–1Pd were conducted on a LEAP™ 3000X HR (Cameca, AMETEK Inc., France) in voltage mode using a specimen temperature of ~80 K, a pulse fraction of 15%, and a constant detection rate of 0.5%. For the alloys Fe–10Mn–3Pd and Fe–10Mn–6Pd, the APT experiments were performed on a LEAP™ 4000X HR (Cameca) in laser mode (355 nm wave length), because premature failure of the specimen occurred with voltage pulsing. The measurements were conducted using a laser energy of 100 pJ, a specimen temperature of ~24 K, and a constant detection rate of 1%. Data processing was performed using the IVAS 3.6.6 software package (Cameca).[27]

## III. RESULTS AND DISCUSSION

### A. Mechanical properties

Figure 1 shows results from tensile tests of Fe–10Mn–1Pd after isothermal aging at 500 °C for different times. In the initial as-quenched condition (solution-heat-treated, SHT), the alloy exhibits a ductile behavior, but brittle failure results in the peak-aged state. However, on prolonged aging, i.e., in the overaged regime, ductility recovers again and the alloy exhibits a similar uniform elongation compared to the SHT condition. The peculiarity of embrittlement and de-embrittlement is discussed in more detail by Moszner et al.[24] Besides that, the yield strength of the material is considerably increased from 662 ± 13 MPa in the as-quenched condition to 1076 ± 6 MPa in the overaged state. Thus, an interesting combination of strength and ductility results in the overaged condition and smaller implant dimensions can be achieved in that case.

Figure 2 presents age-hardening curves for Fe–10Mn–*x*Pd ($x$ = 1, 2, 6), which were isothermally aged at 500 °C for time periods ranging from 5 min up to 1200 h. All alloys show significant age-hardening. The higher the Pd content of the alloys, the higher is the resulting peak-hardness, which shows clearly that Pd participates in the strengthening process. The hardness evolution of the alloys, i.e., a fast increase in hardness until the peak hardness is reached followed by a slow decrease on prolonged aging, is typical of maraging steels.[9,10]

### B. Optical microscopy

For comparison, Fig. 3 presents optical micrographs of the materials in the SHT condition and after aging for 30 h at 500 °C (overaged state). The SHT specimens containing 1 and 3 wt.% Pd [Figs. 3(a) and 3(c)] exhibit the typical lath-martensitic microstructure known from binary Fe–Mn alloys containing 4–10 wt.% Mn.[28,29] SEM investigations of Fe–10Mn–1Pd revealed that the SHT temperature of 1250 °C was sufficient to produce a supersaturated solid solution with a homogenous single-phase microstructure.[10] However, for the steel containing 3 wt.% Pd, the formation of a single-phase microstructure required a homogenization treatment at 1400 °C [Fig. 3(c)]. For Fe–10Mn–6Pd annealed at 1400 °C, a coarse two-phase microstructure is revealed in the OM images [Fig. 3(e)]. The dominating phase exhibits the characteristic lath-martensitic structure similar to Fe–10Mn–1Pd or Fe–10Mn–3Pd, whereas the second phase (dark-contrast in Fig. 3(e)) was only found along some prior austenite grain boundaries. The inset to Fig. 3(e) shows a backscattered electron image of that phase, also revealing a chemical contrast. A lamellar-like structure is visible, and the bright areas are enriched in Pd and Mn. The image indicates partial remelting of the austenite grains due to overheating slightly above solidus, i.e., quenching from the austenite–liquid two-phase field.[30,31] Nevertheless, a homogenous distribution of the alloying elements and a high level of Pd supersaturation can be assumed in the dominating martensitic phase. This results in a higher degree of hardness upon isothermal aging (Fig. 2) and hence a higher volume fraction of the evolving precipitates, which also generates stronger signals from the precipitates in XRD measurements facilitating their phase identification. Compared to the specimens in the SHT condition, a finer microstructure inside the prior austenite grains was observed during over-aging for the alloys investigated [Figs. 3(b), (d), (f)]. This can be ascribed to the formation of reverted austenite[15] and was in particular apparent for Fe–10Mn–1Pd (compare insets to Figs. 3(a) and 3(b)). Table I summarizes the chemical compositions of the alloys determined via EDX-point measurements.

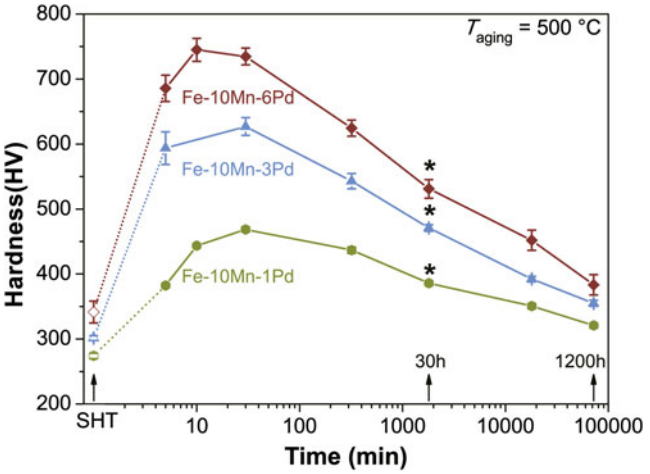


FIG. 2. Hardness as a function of aging time at 500 °C, revealing age-hardening behavior of the alloys investigated, which is typical of maraging steels. The heat-treatment states used for the XRD and APT measurements are indicated by black arrows and stars, respectively.

### C. Atom probe tomography

The APT experiments were conducted to analyze the chemical composition of the precipitates and hence to support the results of the XRD measurements (see section D). Specimens of the alloys in the overaged regime (after aging for 30 h at 500 °C) were investigated via APT. This condition was chosen in particular, as Moszner et al.[10] observed for Fe–10Mn–1Pd that in this state the volume fraction of the precipitates ($f_V$) did not increase any more with progressive aging-time, indicating that $f_V$ has approached an equilibrium value. In addition, the size of the particles was still small enough to fully enclose a few of them in the volume detectable by APT. To illustrate the APT results, cylinders of the same dimension (Ø = 38 nm, height = 40 nm) were cut out of the individual reconstructed volumes. Figure 4(a) presents the atomic positions of Fe (green), Mn (red), and Pd (blue). Enrichment of Mn and Pd at the same areas is clearly visible for all

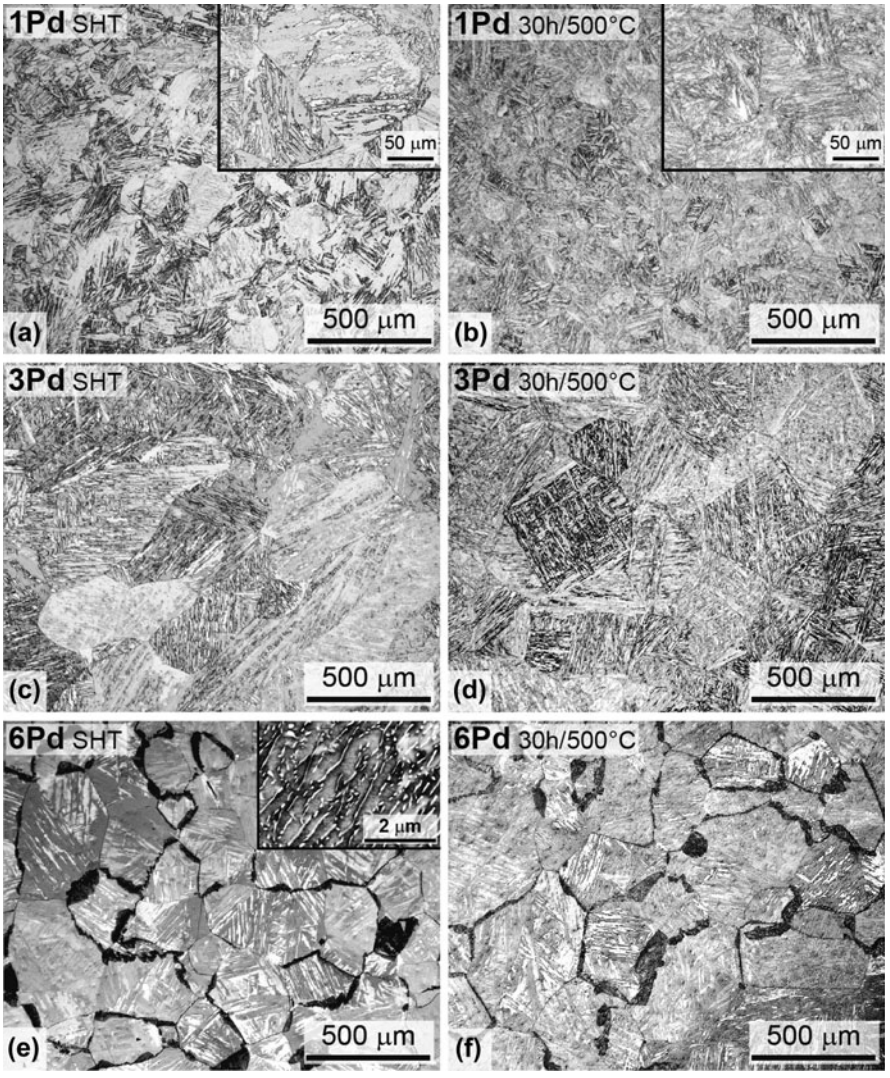


FIG. 3. Optical micrographs of the alloys in the SHT condition and after aging for 30 h at 500 °C: (a, b) Fe–10Mn–1Pd (SHT at 1250 °C); (c, d) Fe–10Mn–3Pd (SHT at 1400 °C); (e, f) Fe–10Mn–6Pd (SHT at 1400 °C), all etched with 1% $HNO_3$. The typical lath-martensitic microstructure is visible for the alloys containing 1 and 3 wt.% Pd. For Fe–10Mn–6Pd, a two-phase microstructure is visible with the lath-martensitic structure dominating. The insets in (a, b) show magnified sections, where a finer microstructure inside the prior austenite grains is apparent for the specimens in the overaged state. The inset in (e) shows a backscattered electron image of the intergranular phase with dark contrast in the optical micrograph.

TABLE I. Nominal and measured (EDX-point measurements) chemical compositions in weight (wt.%) and atomic percent (at.%).

| | | Fe | | Mn | | Pd | |
|---|---|---|---|---|---|---|---|
| Alloy | | wt.% | at.% | wt.% | at.% | wt.% | at.% |
| Fe–10Mn–1Pd | Nominal | 89 | 89.3 | 10 | 10.2 | 1 | 0.5 |
| | EDX | 88.6 | 88.8 | 10.4 | 10.6 | 1.1 | 0.6 |
| Fe–10Mn–3Pd | Nominal | 87 | 88.1 | 10 | 10.3 | 3 | 1.6 |
| | EDX | 86.5 | 87.7 | 10.3 | 10.6 | 3.2 | 1.7 |
| Fe–10Mn–6Pd | Nominal | 84 | 86.3 | 10 | 10.5 | 6 | 3.2 |
| | EDX | 83.4 | 86.0 | 9.9 | 10.4 | 6.7 | 3.6 |

specimens investigated. The composition of the precipitates was determined using the proximity histogram (or proxigram) method.[32] Isoconcentration surfaces[32] (surfaces enclosing a region containing a higher concentration of a selected element compared to a chosen threshold value) were created to delineate the precipitates and to serve as reference surface for the proxigram calculation [Fig. 4(a)]. In a second step, discreet shells with widths of 0.1 nm inside and outside of the isoconcentration surfaces were generated. Each point in the proxigram then corresponds to the concentration of a shell at a defined distance from the isoconcentration surface. By convention, the concentrations at negative distances correspond to shells located outside the isoconcentration surface, which can be used to evaluate the matrix composition. Vice versa, data points at positive distances are related to concentrations inside the isoconcentration surface and hence can be used to assess the composition of the precipitates. Figure 4(b)

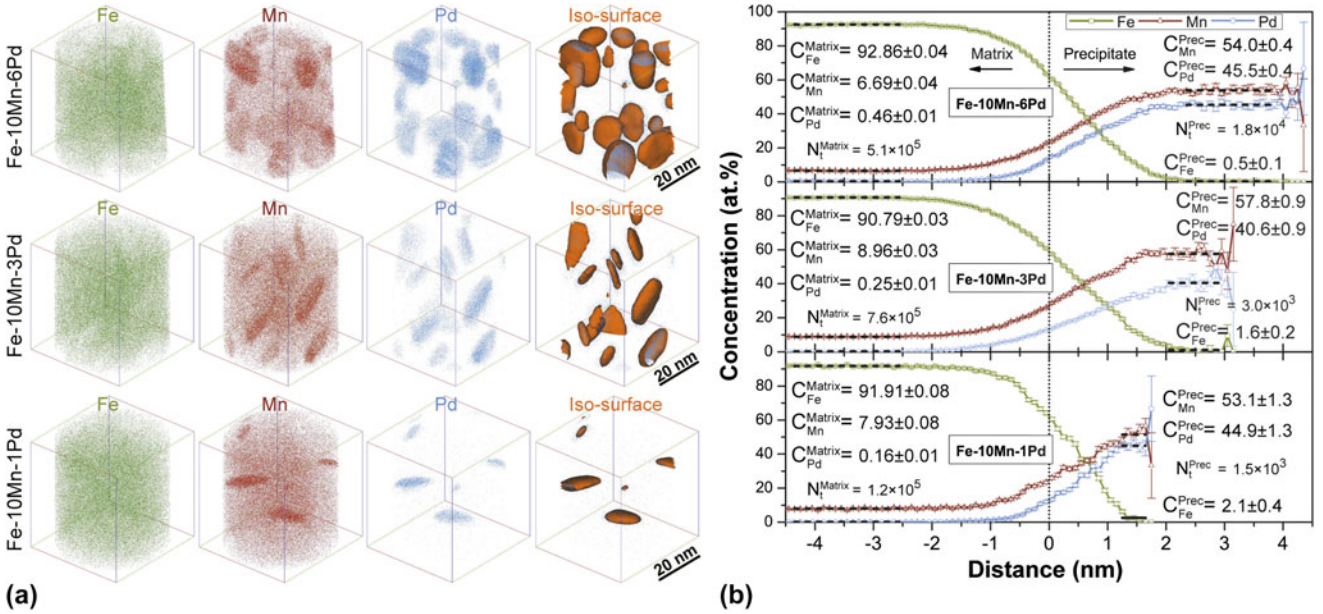


FIG. 4. (a) 3D reconstruction of Fe–10Mn–*x*Pd alloys ($x$ = 1, 3, 6) after aging for 30 h at 500 °C, showing the atomic positions of Fe (green), Mn (red), Pd (blue), and isoconcentration surfaces for regions containing >35 at.% Mn + Pd (orange). (b) Proxigrams for Fe, Mn, and Pd corresponding to a Mn + Pd isoconcentration of 35 at.%. The dashed black lines indicate the data points used to evaluate the composition of the matrix ($C^{\mathrm{Matrix}}$) and of the precipitates ($C^{\mathrm{Prec}}$). The total numbers of atoms considered for the concentration measurements of the matrix $\left(N_{\mathrm{t}}^{\mathrm{Matrix}}\right)$ and of the precipitates $\left(N_{\mathrm{t}}^{\mathrm{Prec}}\right)$ are also given. For all alloys, the precipitates are nearly free of Fe and mainly consist of Mn and Pd, indicating that a Mn–Pd intermetallic phase has formed.

presents the results of the proxigrams (only precipitates fully enclosed within the reconstructed volume were considered) for the investigated specimens aged for 30 h at 500 °C. The proxigrams were calculated using an isoconcentration surface of Mn + Pd set to a threshold value of 35 at.% (average inflection point of the Mn + Pd concentration taking into account the three datasets). The black dashed lines in the proxigrams indicate the data points used to calculate the concentration of the elements within the matrix ($C^{\mathrm{Matrix}}$) and within the precipitates ($C^{\mathrm{Prec}}$), and the corresponding values are depicted in each graph. According to Miller et al.[26] the concentration in at.% of each element ($C_i$) was calculated by $C_i = N_i/N_{\mathrm{t}}$, where $N_i$ is the number of atoms of the corresponding species $i$ and $N_{\mathrm{t}}$ is the total number of atoms considered. The errors were estimated by the standard deviation $\sigma_i = \sqrt{C_i(1-C_i)/N_{\mathrm{t}}}$. Similar concentration profiles were obtained for all three alloys. The Pd content of the matrix nearly decreases to zero, reflecting the fact that most of the Pd is confined within the particles. The precipitates are nearly free of Fe and mainly consist of Mn and Pd, thus indicating a Mn–Pd intermetallic character of the hardening phase. According to the binary Mn–Pd phase diagram,[33] two intermetallic phases, β and $\beta_1$, can be considered here with respect to the measured composition of the precipitates. Both phases exist over a wide compositional range (β = 39 ≤ Pd at.% ≤ 66, $\beta_1$ = 47 ≤ Pd at.% ≤ 68), at which β only occurs above 540 °C, whereas $\beta_1$ also exists below that temperature. However, Okamoto[33] noted that the true equilibrium phase diagram is still unknown and hence the exact boundaries of the phases need to be considered with care.

### D. X-ray diffraction

Figure 5 displays the XRD patterns of the alloys investigated in the SHT state, and subjected to aging at 500 °C for 30 h and 1200 h. In the SHT condition, the samples containing 1 and 3 wt.% Pd only reveal the presence of bcc diffraction lines. For Fe–10Mn–6Pd, in addition to strong bcc reflections, a weak peak at around 40.2° is visible (insert in Fig. 5(a)), which can be ascribed to the observed intergranular second phase [Fig. 3(c)]. Since the specimen was rapidly quenched from 1400 °C, the weak x-ray peak can be attributed to the high-temperature phase β-MnPd, which may also have undergone a phase transformation to $\beta_1$-MnPd. It can be calculated that the reflection with the highest intensity of the β- and $\beta_1$-phase must in both cases be located at around 40°. However, no further peaks of the intergranular phase were distinguished in the XRD spectra of the SHT condition, which hampers clear identification.

For the specimens subjected to aging at 500 °C, peaks related to austenite (γ), epsilon martensite (ε), and also to the evolved precipitates were clearly observable besides bcc diffraction lines (Fig. 5). Considering first the formation of γ and ε, it is known from Ni-based maraging steels that during aging treatment partial reversion from martensite

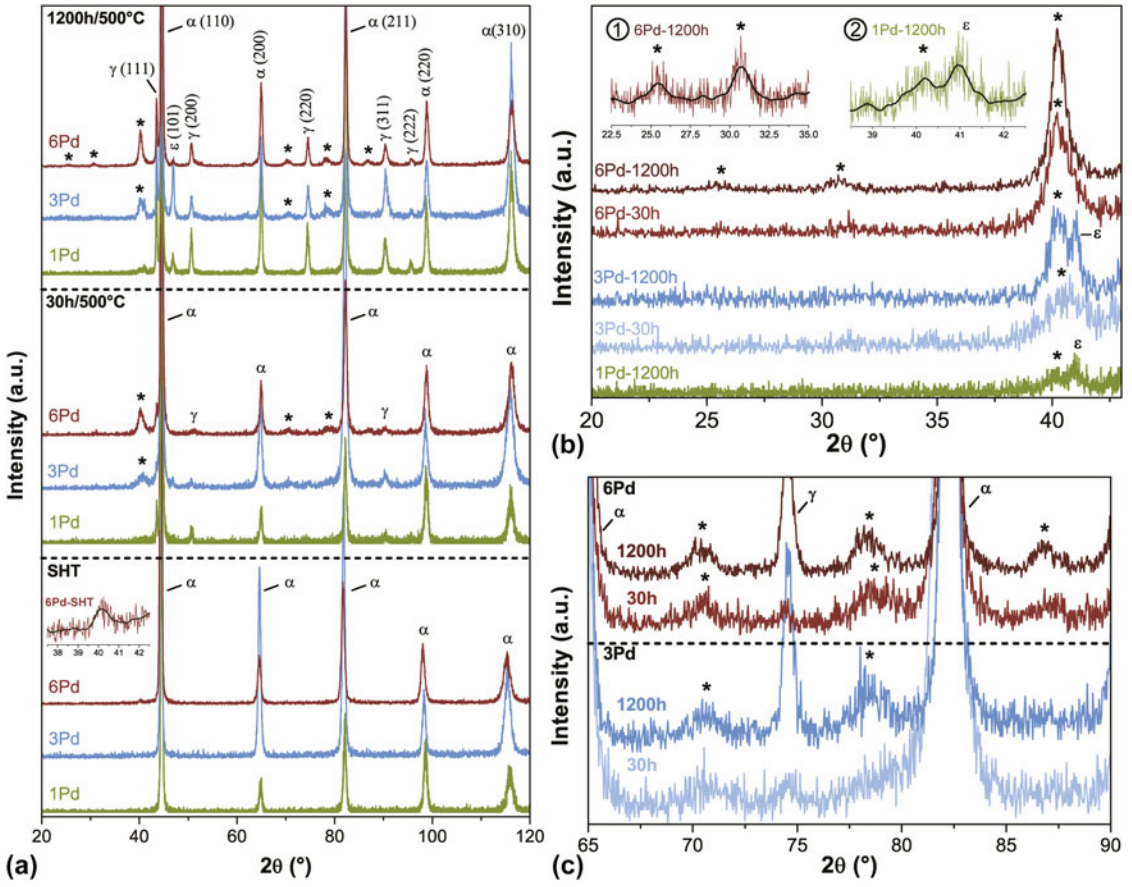


FIG. 5. XRD results of Fe–10Mn–*x*Pd alloys ($x$ = 1, 3, 6) in the SHT condition and after aging for 30 h and 1200 h at 500 °C. (a) Overview; (b) and (c) detailed sections at small and high angles. The spectra were normalized with respect to the highest value of each measurement; the stars indicate the positions related to evolving precipitates; the black lines in the inserts represent guidelines for the eye.

($\alpha'$) to γ occurs in the α + γ phase region.[9,34] This type of γ is often referred to as reverted γ, and the formation mechanism is associated with a diffusional process leading to an enrichment of Ni within the reverted γ.[34] The martensite start temperature ($M_s$) depends strongly on composition, and it decreases with increasing Ni content.[35] Consequently, due to Ni enrichment, the reverted γ gets stabilized upon quenching to room temperature (RT). The Fe–Mn system features transformation characteristics similar to those of Fe–Ni alloys.[29,36] However, in the Fe–Mn system, ε-martensite occurs in the compositional range between 10 and 27 wt.% Mn.[36,37] Hence, it can be concluded for the alloys investigated here that during aging at 500 °C reverted γ enriched in Mn evolves, and upon quenching to RT is partially transformed to ε-martensite. Peaks related to the evolving precipitates can be observed in the XRD patterns of Fe–10Mn–3Pd and Fe–10Mn–6Pd (indicated by stars in Fig. 5) after just 30 h of aging, and on further aging for 1200 h they become even more clearly visible. Figures 5(b) and 5(c) show enlarged sections of the corresponding angular ranges. For Fe–10Mn–1Pd only a weak peak corresponding to the precipitates is observable (insert 2 in Fig. 5(b)) after 1200 h of aging. APT measurements reveal that the precipitates consist mainly of Mn and Pd and, due to their composition, can be related to the β- or $\beta_1$-MnPd intermetallic phase.

Table II summarizes the peak positions of the precipitates observed in the XRD patterns of the specimens aged for 1200 h at 500 °C, and also lists the 2θ values for β and $\beta_1$. The observed reflections of the precipitates only match the $\beta_1$ phase. Some of the expected reflections of the $\beta_1$ phase were, however, not revealed, as they either showed an overlap with the α, γ, or ε phases or because their relative intensity is very low. The combined results of the APT and XRD measurements confirm that in the Fe–Mn–Pd maraging steels, as also in Fe–Mn-based systems containing Ni or Pt, the precipitates in the overaged state exhibit an ordered fct structure which corresponds to the intermetallic phase near the equiatomic composition of the respective Mn–X (X = Ni, Pd, Pt) binary phase diagrams. Table III summarizes the lattice parameters of the precipitates in the different ternary maraging steels, and those of the corresponding intermetallic binary phases. A good agreement is observed and the lattice parameters of the precipitates differ by an average of only 1% from the equilibrium values of the corresponding binary phases.

TABLE II. Peak positions (2θ in°) of the precipitates observed in the XRD spectra of specimens aged for 1200 h at 500 °C (Fig. 5) and calculated for the fct $\beta_1$-MnPd phase with $a = 0.411$ nm and $c = 0.351$ nm, and for the bcc β-MnPd phase with $a = 0.315$ nm. The relative intensities are given in parentheses.

| Fe–10Mn–1Pd | Fe–10Mn–3Pd | Fe–10Mn–6Pd | $\beta_1$-MnPd | β-MnPd |
|---|---|---|---|---|
| | | 25.5 | 25.4 (10) | 28.3 (15) |
| | | 30.7 | 30.7 (12) | |
| 40.2 | 40.3 | 40.3 | 40.2 (100) | 40.4 (100) |
| | | | 43.9 (38) | |
| | | | 51.3 (5) | 50.1 (4) |
| | | | 52.2 (11) | |
| | ... | ... | 61.8 (3) | 58.8 (15) |
| | | | 64.2 (11) | 66.2 (5) |
| | | | 70.2 (2) | |
| | 70.5 | 70.4 | 70.2 (16) | 73.3 (28) |
| | | | 72.7 (2) | |
| | 78.9 | 78.4 | 78.3 (22) | |
| | | 86.9 | 86.9 (8) | 87.9 (8) |

TABLE III. Comparison of lattice parameters determined via XRD for the intermetallic particles in the different ternary maraging systems, and those of the fct phase of the respective binary phase diagrams.

| System | $a$ (nm) | $c$ (nm) | References |
|---|---|---|---|
| Fe–6Mn–12Ni, (1000 h at 450 °C) | 0.3734 | 0.3512 | 14 |
| θ-NiMn | 0.369 | 0.349 | 38 |
| Fe–9Pt–9Mn, (500 h at 500 °C) | 0.401 | 0.368 | 12 |
| $\beta_1$-MnPt | 0.4002 | 0.3660 | 39 |
| Fe–10Mn–3Pd (1200 h at 500 °C) | 0.410 | 0.352 | Present work |
| Fe–10Mn–6Pd (1200 h at 500 °C) | 0.411 | 0.351 | Present work |
| $\beta_1$-MnPd | 0.4069 | 0.3585 | 40 |

## IV. SUMMARY

In this study, the precipitates that form during aging at 500 °C in Fe–Mn–Pd maraging steels were characterized using APT and XRD. Alloys containing 1, 3, and 6 wt.% Pd with a fixed Mn content of 10 wt.% were investigated. The steels exhibit considerable hardening upon aging. APT results in combination with XRD measurements reveal that the precipitates in the overaged state consist mainly of Mn and Pd and can be related to the fct $\beta_1$-MnPd intermetallic phase, which is similar to what has been observed for Fe–Mn–Ni and Fe–Mn–Pt maraging steels.

## ACKNOWLEDGMENTS

The authors thank N. Kränzlin for support with the XRD measurements and M. Schinhammer and E. Fischer for help with the sample preparation; and acknowledge the support of the Electron Microscopy Center of ETH Zurich (EMEZ). The authors appreciate the financial support received in the framework of the project "Bio Compatible Materials and Applications – BCMA" initiated by the Austrian Institute of Technology GmbH (AIT).

## REFERENCES

1. H. Hermawan, D. Dube, and D. Mantovani: Development of degradable Fe-35Mn alloy for biomedical application. In *5th International Conference on Processing and Manufacturing of Advanced Materials (Thermec 2006 Supplement)*, T. Chandra, K. Tsuzaki, M. Militzer, and C. Ravindran ed.; Trans Tech Publications Ltd: Zurich, 2007; p. 107.
2. M. Schinhammer, A.C. Hänzi, J.F. Löffler, and P.J. Uggowitzer: Design strategy for biodegradable Fe-based alloys for medical applications. *Acta Biomater.* **6**(5), 1705 (2010).
3. M. Peuster, P. Wohlsein, M. Brugmann, M. Ehlerding, K. Seidler, C. Fink, H. Brauer, A. Fischer, and G. Hausdorf: A novel approach to temporary stenting: Degradable cardiovascular stents produced from corrodible metal - results 6-18 months after implantation into New Zealand white rabbits. *Heart* **86**(5), 563 (2001).
4. M. Peuster, C. Hesse, T. Schloo, C. Fink, P. Beerbaum, and C. von Schnakenburg: Long-term biocompatibility of a corrodible peripheral iron stent in the porcine descending aorta. *Biomaterials* **27**(28), 4955 (2006).
5. R. Waksman, R. Pakala, R. Baffour, R. Seabron, D. Hellinga, and F.O. Tio: Short-term effects of biocorrodible iron stents in porcine coronary arteries. *J. Interv. Cardiol.* **21**(1), 15 (2008).
6. H. Hermawan, A. Purnama, D. Dube, J. Couet, and D. Mantovani: Fe-Mn alloys for metallic biodegradable stents: Degradation and cell viability studies. *Acta Biomater.* **6**(5), 1852 (2010).
7. T. Huang, J. Cheng, and Y.F. Zheng: In vitro degradation and biocompatibility of Fe–Pd and Fe–Pt composites fabricated by spark plasma sintering. *Mater. Sci. Eng. C* **35**(0), 43 (2014).
8. M. Schinhammer, I. Gerber, A.C. Hänzi, and P.J. Uggowitzer: On the cytocompatibility of biodegradable Fe-based alloys. *Mater. Sci. Eng. C* **33**(2), 782 (2013).
9. R.F. Decker and S. Floreen: Maraging steels - The first 30 years. In *Maraging Steels: Recent Developments and Applications*, TMS-AIME, Warrendale, 1988; p. 1.
10. F. Moszner, A.S. Sologubenko, M. Schinhammer, C. Lerchbacher, A.C. Hänzi, H. Leitner, P.J. Uggowitzer, and J.F. Löffler: Precipitation hardening of biodegradable Fe-Mn-Pd alloys. *Acta Mater.* **59**(3), 981 (2011).
11. V.M. Kardonskii and M.D. Perkas: Aging of martensite in Fe−Ni−Mn steels. *Met. Sci. Heat Treat.* **8**(4), 254 (1966).
12. M. Tanaka and T. Suzuki: On the age-hardening of Fe-Pt-Mn alloys. *J. Jpn. Inst. Met.* **35**(10), 974 (1971).
13. D.R. Squires and E.A. Wilson: Aging and brittleness in an Fe-Ni-Mn alloy. *Metall. Trans.* **3**(2), 575 (1972).
14. M. Yodogawa: Precipitation behavior in Fe-Ni-Mn martensitic alloys. *Trans. Jpn. Inst. Met.* **17**(12), 799 (1976).
15. L.T. Shiang and C.M. Wayman: Maraging behavior in an Fe–19.5Ni–5Mn alloy. 1. Precipitation characteristics. *Metallography* **21**(4), 399 (1988).
16. S.N. Basu and A.N. Kumar: Enhanced tensile ductility in Fe-Mn-Ni base maraging alloys. *Mater. Sci. Eng. A* **122**(2), L5 (1989).
17. S-J. Kim and C.M. Wayman: Electron microscopy study of precipitates in Fe-Ni-Mn maraging alloys. *Mater. Sci. Eng. A* **136**, 121 (1991).
18. S. Hossein Nedjad, M. Nili Ahmadabadi, T. Furuhara, and T. Maki: High resolution transmission electron microscopy study on the nano-scale twinning of θ-NiMn precipitates in an Fe–Ni–Mn maraging alloy. *Physica Status Solidi A* **203**(9), 2229 (2006).
19. S.H. Nedjad, M.R.M. Garabagh, M.N. Ahmadabadi, and H. Shirazi: Effect of further alloying on the microstructure and mechanical properties of an Fe-10Ni-5Mn maraging steel. *Mater. Sci. Eng. A* **473**(1–2), 249 (2008).
20. R.K. Ray and A.K. Seal: Structure and strength of 2 age-hardenable Fe-Mn-Ni alloys. *Scr. Metall.* **10**(11), 971 (1976).

21. N.H. Heo: Ductile-brittle-ductile transition and grain boundary segregation of Mn and Ni in an Fe-6Mn-12Ni alloy. *Scr. Mater.* **34**(10), 1517 (1996).
22. J. Singh and C.M. Wayman: Age-hardening characteristics of a martensitic Fe-Ni-Mn alloy. *Mater. Sci. Eng.* **94**, 233 (1987).
23. T. Suzuki: Precipitation hardening in maraging steels - martensitic ternary iron-alloys. *Trans. Iron Steel Inst. Jpn.* **14**(2), 67 (1974).
24. F. Moszner, S.S.A. Gerstl, P.J. Uggowitzer, and J.F. Löffler: Atomic-scale characterization of prior austenite grain boundaries in an Fe–Mn-based maraging steel using site-specific atom-probe tomography. *Acta Mater.* (2014). DOI: 10.1016/j.actamat.2014.04.009.
25. EN 10002–10011: *Standard Metallic Materials - Tensile Testing - Part 1: Method of Testing at Ambient Temperature* (DIN, Berlin, 2001).
26. M.K. Miller and R.G. Forbes: Atom probe tomography. *Mater. Charact.* **60**(6), 461 (2009).
27. D. Larson, T. Prosa, R. Ulfig, B. Geiser, and T. Kelly: *Local Electrode Atom Probe Tomography* (Springer, New York, 2013).
28. M.J. Roberts: Effect of transformation substructure on strength and toughness of Fe-Mn alloys. *Metall. Trans.* **1**(12), 3287 (1970).
29. J.D. Bolton and E.R. Petty: The transformation behaviour of low-carbon iron-manganese alloys. *Met. Sci. J.* **5**, 166 (1971).
30. W. Püttgen, B. Hallstedt, W. Bleck, and P.J. Uggowitzer: On the microstructure formation in chromium steels rapidly cooled from the semi-solid state. *Acta Mater.* **55**(3), 1033 (2007).
31. H. Schumann and H. Oettel: *Metallography* (Wiley-VCH, Weinheim, 2005), p. 665.
32. O.C. Hellman, J.A. Vandenbroucke, J. Rusing, D. Isheim, and D.N. Seidman: Analysis of three-dimensional atom-probe data by the proximity histogram. *Microsc. Microanal.* **6**(5), 437 (2000).
33. H. Okamoto: Mn-Pd (manganese-palladium). *J. Phase Equilib.* **14**(5), 654 (1993).
34. R. Schnitzer, R. Radis, M. Nöhrer, M. Schober, R. Hochfellner, S. Zinner, E. Povoden-Karadeniz, E. Kozeschnik, and H. Leitner: Reverted austenite in PH 13-8 Mo maraging steels. *Mater. Chem. Phys.* **122**(1), 138 (2010).
35. C. Servant and P. Lacombe: Structural transformations produced during tempering of Fe-Ni-Co-Mo alloys. *J. Mater. Sci.* **12**(9), 1807 (1977).
36. H. Schumann: Martensitic transformations in low carbon manganese steels. *Arch. Eisenhüttenwes.* **38**(8), 647 (1967).
37. J. Martínez, S.M. Cotes, A.F. Cabrera, J. Desimoni, and A. Fernández Guillermet: On the relative fraction of ε martensite in γ-Fe–Mn alloys. *Mater. Sci. Eng. A* **408**(1–2), 26 (2005).
38. V.E. Egorushkin, S.N. Kulkov, and S.E. Kulkova: Electronic-structure and the theory of phase-transformations in NiMn. *Physica B & C* **123**(1), 61 (1983).
39. K. Brun, A. Kjekshus, and W.B. Pearson: Equiatomic transition metal alloys of manganese. I. Tetragonal PtMn phase. *Philos. Mag.* **10**(104), 291 (1964).
40. A. Kjekshus, R. Mollerud, A.F. Andresen, and W.B. Pearson: Equiatomic transition metal alloys of manganese. 6. Structural and magnetic properties of Pd-Mn phases. *Philos. Mag.* **16**(143), 1063 (1967).